International Journal of Computer Information Systems and Industrial Management Applications
ISSN 2150-7988 Volume 18 (2026) pp. 1-22

https://doi.org/10.70917/ijcisim-2026-0146
Article

Research on stability analysis and control optimization method of DC microgrid based on numerical simulation

Fanhua Meng, Likui Yi *, Rui Feng and Dongge Liu

School of Electric Power, Shenyang Institute of Engineering, Shenyang, Liaoning, 110136, China;
18624026728@163.com

Abstract: DC microgrid systems can better meet power energy demands and adapt to the future development characteristics of DC loads. Based on the structure of DC microgrids, this paper combines the operational characteristics of distributed power sources (wind power generation, solar power generation) to establish a mathematical model of the DC microgrid system. By introducing droop control into AVDCM control, fuzzy control is configured to use only the rate of change of bus voltage as input, forming an improved P-U droop coordinated AVDCM control. This establishes a control optimization model for the DC microgrid system. DC microgrid control optimization simulation experiments were conducted to explore the control optimization performance of the proposed DC microgrid control optimization model. Under grid-connected operation, both the 700V DC bus voltage and the 48V DC bus voltage can recover to a voltage-stable state within 0.1 seconds. In islanded operation, the output power of the photovoltaic panels rises to between 144 kW and 146 kW within approximately 0.7 seconds, reducing the power supply burden on the batteries. Under varying 700 V DC bus voltages, the load can operate reliably, and the 48 V DC bus voltage remains in a steady state.

Keywords: DC microgrid; AVDCM control; fuzzy control; P-U droop coordination

1. Introduction

As users increasingly prioritize power supply reliability and power quality, and with the widespread adoption of various forms of renewable energy such as solar and wind power, microgrids have garnered significant attention from scholars as an effective means of integrating distributed power sources into the grid [1-3]. Various distributed power sources in microgrids, such as photovoltaic cells, supercapacitors, and wind turbines, primarily output direct current (DC) or involve DC intermediate stages. Additionally, many household appliances and office equipment inherently require DC power to function properly [4-5]. Therefore, if microgrids adopt DC as the form of energy transmission, it can reduce conversion stages and enhance energy utilization efficiency [6-7]. In recent years, DC microgrids have gradually emerged as a new research direction in microgrid technology due to their unique advantages, offering broad application prospects in residential buildings, data centers, and electric vehicle charging stations [8].

A DC microgrid system is a grid configuration that integrates distributed power sources, energy storage, and loads, connected to the external AC grid via one or more DC-AC converters [9]. Based on the operating mode of the interface converter, DC microgrids can operate in two modes: in grid-connected mode, the microgrid system exchanges energy bidirectionally with the main grid [10]; in standalone mode, the DC microgrid functions as an independent power supply system capable of stable operation [11]. Distributed power sources and various loads in the DC microgrid are connected to the DC bus via corresponding AC-DC and DC-DC converters [12]. These parallel power electronic devices ensure the normal and stable operation of the DC microgrid system through mutual coordination and control.

Currently, research on DC microgrids primarily focuses on five aspects: system topology, system optimization planning, operational control strategies, protection and communication technologies, and

stability analysis [13]. Among these, stability analysis provides a reference for the reliable operation of DC microgrids and theoretical support for subsequent control parameter design and optimization [14-15]. Reference [16] established a large-signal model for an independently operating DC microgrid, providing a stability criterion for system parameter design. However, the paper overlooked the influence of the control system on the equivalent model. Reference [17] studied virtual inertia control to limit continuous charging of energy storage units in battery overcharging and over-discharging issues during DC microgrid island operation. However, this paper primarily focused on overall coordinated control and did not provide a detailed analysis of virtual inertia control. Reference [18] proposes a comprehensive stability assessment for a DC microgrid with high penetration, employing eigenvalue analysis to investigate the effects of system DC feeder length, bus capacitance, and droop controllers on system stability.

The stability of DC bus voltage is a critical issue in DC microgrid systems, and ensuring the stability of DC bus voltage is a prerequisite for DC microgrid control. Depending on the degree of disturbance, the stability of DC microgrids can be divided into two categories: small-signal stability and large-signal stability [19]. Small-signal stability refers to the stability of the DC microgrid under small disturbances. Near the operating equilibrium point, approximate linearization methods can be used, along with eigenvalue analysis or impedance analysis, to assess system stability [20-21]. Literature [22] proposes a design and stability analysis scheme combining an independent solar photovoltaic system with a DC microgrid, focusing on achieving efficiency, stability, and optimization of the DC microgrid through various components and technologies. Reference [23] addresses the instability caused by constant power loads in DC microgrids with multiple DC-DC converters, proposing two stability methods for constant voltage source mode and droop mode, while providing the necessary conditions for stability and verifying the feasibility of these methods through numerical simulations. Literature [24] analyzes the stability of DC microgrids and the factors influencing stability, proposing a frequency-based virtual impedance method to enhance damping effects, and verifying its feasibility through numerical simulations. Literature [25] investigates a control method based on modifying the converter output impedance to improve the transient response of DC microgrids, which includes a virtual capacitor and a virtual inductor. Although the above methods improve the stability margin of the DC bus, they are only applicable to single-bus DC buses.

The large disturbance stability of a microgrid primarily refers to the ability of the microgrid system to maintain a stable operating state when faced with significant external disturbances or internal faults [26]. According to current research, large-signal stability analysis methods can be categorized into three main types: phase portrait method, equal area criterion, and Lyapunov stability theorem. The Lyapunov stability theorem is considered one of the most effective methods for analyzing the large-signal stability of nonlinear systems, and corresponding research has been conducted on this topic [27]. Literature [28] introduced the Lyapunov stability theorem to analyze the transient stability of voltage-source converter (VSC) systems, and the Lyapunov function serves as the foundation of the Lyapunov stability theorem. Reference [29] proposes an adaptive active control method to suppress low-frequency oscillations in DC microgrids, adjusting the damping coefficient of the virtual impedance loop, and using small-signal analysis during the tuning process to determine the initial adjustment of the damping coefficient. Reference [30] employs the phase plane method for large-signal stability analysis of a phase-locked synchronous voltage-source converter, proposing an adaptive phase-locked loop capable of switching between first-order and second-order modes during transient periods with large disturbances. However, the impact of control delays is not considered. Reference [31] employs a hybrid potential function method to analyze the stability of a DC microgrid with filters and a Constant Power Load (CPL), and calculates the system's large-signal stability criteria. For DC microgrid systems, large-signal stability analysis methods are still not fully developed and require further research.

This paper establishes a DC microgrid system, defines the structure of the DC microgrid system, and constructs a mathematical model of the energy storage system based on the mathematical models of wind turbines and photovoltaic cells in the DC microgrid. A mathematical model of the DC microgrid system is established. Small-signal models are developed for various converters, including the grid-side converter, wind turbine-side converter, and battery-side converter. Considering that traditional P-U droop dual-loop control lacks inertia characteristics and dynamic performance issues, it is incorporated into AVDCM control, and the droop control is improved to establish a DC microgrid control optimization model based on P-U droop. The rate of change of bus voltage is used as the input to avoid the mutual influence between power and photovoltaic module output power in P-U droop. Using a DC microgrid with virtual inertia control as a comparison object, stability simulation experiments were conducted on the DC microgrid to verify the stability performance of the proposed P-U droop-based DC microgrid control optimization model. Additionally, DC microgrid control optimization simulation experiments were conducted to explore the control optimization performance of the proposed control

optimization model under both grid-connected and islanded operation modes.

2. Modeling of DC Microgrid Systems

DC microgrids are one of the future development directions for power grids. Their main components include distributed power sources (such as wind power generation and solar power generation), energy storage devices (such as batteries, supercapacitors, and flywheels), various loads, converters, switches, and transmission lines. This chapter primarily analyzes the operational characteristics of distributed power sources (wind power generation, solar power generation) and energy storage systems (batteries, supercapacitors) in DC microgrids, establishes their mathematical models, and provides a model foundation for subsequent discussions.

2.1. Structure of DC Microgrids

The structure of the DC microgrid established in this paper is shown in Figure 1, which mainly consists of wind power generation units, photovoltaic power generation units, energy storage systems, DC loads, AC loads, and AC distribution grids [32]. The wind power generation unit and photovoltaic power generation unit only output power, connected to the DC bus via their respective unidirectional converters. The energy storage system serves to balance power, connected to the DC bus via a bidirectional DC/DC converter. Loads include DC loads and AC loads, with the DC bus supplying power to the loads via their respective converters. The entire DC microgrid system is connected to the AC distribution grid via a bidirectional DC/AC converter.

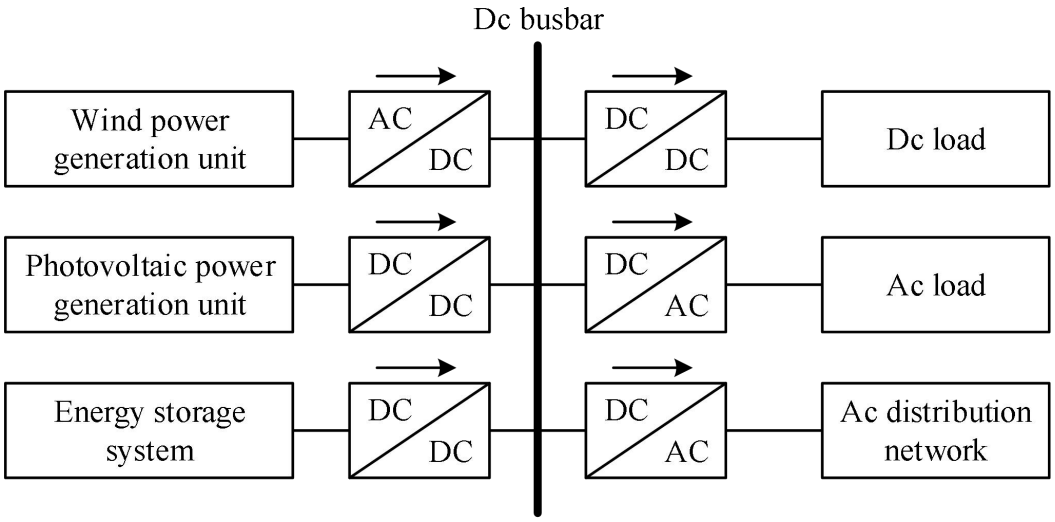

Figure 1. DC microgrid structure.

2.2. Distributed Power Source Model

2.2.1. Wind Power Generation System Model

Wind power generation is the most important form of distributed power generation. Its technology has matured to date, and its commercial development value is also relatively high among renewable energy sources. The main components of a wind power generation system include blades, gearboxes, rectifiers, inverters, and alternating current generators. When the wind blows, it causes the blades to rotate, generating mechanical energy. The rotational speed of the turbine blades is increased through the gearbox, thereby driving the generator. The mechanical energy is ultimately converted into electrical energy through the wind-powered AC generator.

Based on the principle of wind power generation, it can be seen that the output power of a wind power generation system is primarily related to wind speed. The relationship between wind speed and power can be described by formulas (1) to (3):

$$P_{wt} = \begin{cases} 0 & v < v_{ci} \\ k_1 v^3 - k_2 P_r & v_{ci} \le v \le v_r \\ P_r & v_r < v < v_{co} \\ 0 & v \ge v_{co} \end{cases} \quad (1)$$

$$k_1 = \frac{p_r}{v_r^3 - v_{ci}^3} \tag{2}$$

$$k_2 = \frac{v_{ci}^3}{v_r^3 - v_{ci}^3} \tag{3}$$

In the formula:

P_{wt} — Actual output power of the wind turbine, unit: kW;

v — Real-time wind speed at the location of the wind turbine, unit: m/s;

v_{ci} — Cut-in wind speed of the wind turbine, unit: m/s;

v_r — Rated wind speed of the wind turbine, unit: m/s;

v_{co} — Cut-out wind speed of the wind turbine, unit: m/s;

P_r — the rated power of the wind turbine, in kW.

2.2.2. Photovoltaic Power Generation System Model

The basic principle of photovoltaic power generation is that when solar panels are exposed to sunlight, a certain potential difference is generated inside them due to their structural characteristics. Solar cells utilize this potential difference to directly convert solar energy into electrical energy. Therefore, solar panels are the key energy conversion devices in photovoltaic power generation systems.

Light intensity and ambient temperature have a significant impact on the operating characteristics of solar cells. The actual output power of a photovoltaic power generation system can be expressed by formula (4):

$$P_{PV} = f_{PV} Y_{PV} \left(\frac{I_T}{I_S} \right) \left[1 + \alpha_{PV} (T_{cell} - T_{cell,STC}) \right] \tag{4}$$

In the formula:

P_{FV} — Actual active power output of the solar cell, in kW;

f_{PV} — Photovoltaic derating factor, indicating the impact of pollutants or other factors on the solar panel that cause shading and affect the output power of photovoltaic power generation, typically taken as 0.8;

Y_{PV} — the rated capacity of the solar cell, i.e., the output power of the photovoltaic array measured under standard test conditions, in kW;

I_τ — the solar irradiance intensity around the photovoltaic array measured under actual environmental conditions, in kW/m²;

I_s — the solar radiation intensity measured under standard test conditions, taken as 1 kW/m²;

α_{PV} — Power temperature coefficient of the solar cell, typically taken as -0.47%/°C;

T_{cell} — Operating temperature of the solar cell panel, in °C, generally taken as 47°C when the photovoltaic array can receive solar radiation;

$T_{cell,STC}$ — Temperature of the solar cell under standard test conditions, generally taken as 25°C.

From equation (4), it can be seen that once the model of the solar cell in the photovoltaic system is determined, the rated capacity of the photovoltaic system is also determined. In the formula, only I_T remains as an unknown quantity, indicating that the output power of the photovoltaic cell at this time is solely dependent on I_T.

2.3. Energy Storage System Model

In a DC microgrid system, while renewable energy generation can meet economic and environmental requirements compared to traditional fossil fuel-based power generation, renewable energy generation is susceptible to external environmental influences, exhibiting randomness and indirectness, and fluctuations in load can also impact the system. Therefore, energy storage devices must be integrated into the system. When renewable energy generation is sufficient, excess electricity is stored in the energy

storage system to enhance renewable energy utilization. When renewable energy generation is insufficient, the stored energy is used to compensate for the shortfall, ensuring the system operates safely and stably.

There are various types of energy storage devices, and different storage methods have distinct performance characteristics and application ranges. Common energy storage devices include the following categories: battery storage, flywheel storage, pumped storage, compressed air storage, supercapacitors, and superconducting magnetic storage.

2.3.1. Battery Model

There are many types of batteries used in energy storage systems. Compared to other types of batteries such as all-fluoride flow batteries and lithium-ion batteries, lead-acid batteries are widely used due to their relatively mature technology and lower cost. Common equivalent circuit models for storage batteries.

The mathematical model for charging and discharging energy storage batteries can be expressed by equation (5):

$$\begin{cases} SOC(t) = SOC(t-1) + m_{ES}(t)\dfrac{P_{ES}(t)\Delta t\eta_c}{ESS_R}, m_{ES}(t) = -1 \\ SOC(t) = SOC(t-1) - m_{ES}(t)\dfrac{P_{ES}(t)\Delta t}{ESS_R\eta_d}, \quad m_{ES}(t) = 1 \end{cases} \tag{5}$$

In the equation:

$SOC(t-1)$ — State of charge of the energy storage battery at time $t-1$;

$SOC(t)$ — State of charge of the energy storage battery at time t;

$P_{ES}(t)$ — Charging/discharging power of the energy storage battery at time t, in kW;

η_c — Charging efficiency of the energy storage battery at time t;

η_d — Discharging efficiency of the energy storage battery at time t;

$m_{Es}(t)$ — the charge/discharge state determination coefficient of the energy storage battery at time t, with values of -1 or 1. When $m_{ES}(t) = -1$, it indicates a charging state, with $P_{ES} < 0$; when $m_{ES}(t) = 1$, it indicates a discharging state, with $P_{ES} > 0$;

ESS_R — the rated capacity of the energy storage battery, in kWh;

Δt — the time interval.

2.3.2. Supercapacitor Model

The leakage resistance R in the equivalent model represents the loss caused by extremely small leakage currents within the electrolyte when the supercapacitor is in a self-discharge state. This typically only affects long-term energy storage processes. The time constant of the supercapacitor's self-discharge circuit is significantly longer than its charge-discharge time constant, often lasting tens of hours or even hundreds of hours. In practical applications, supercapacitors are typically connected to a power source and undergo rapid and frequent charge-discharge cycles, especially when connected via a power converter. Therefore, the leakage resistance R can generally be neglected. The equivalent series inductance L is generated during the manufacturing process and can generally be neglected, especially when the output current changes slowly.

According to circuit laws, the mathematical relationship for a simple series RC model is:

$$U = I_C R_{ESR} + \frac{1}{C}\int I_C dt \tag{6}$$

The state of charge (SOC) of the supercapacitor is:

$$SOC = \frac{Q}{Q_N} = \frac{C(U_c - U_{\min})}{C(U_{\max} - U_{\min})} = \frac{U_0 + \frac{1}{C}\int_0^t I_C dt - U_{\min}}{U_{\max} - U_{\min}} \tag{7}$$

The energy stored in supercapacitors is:

$$W = \frac{1}{2} C(U_{\max}^2 - U_{\min}^2) \tag{8}$$

In Equations (6) to (8):

Q — actual charge of the supercapacitor;

Q_N — maximum charge of the supercapacitor;

$U_{\max}$ — maximum operating voltage of the supercapacitor;

$U_{\min}$ — minimum operating voltage of the supercapacitor;

U_0 — initial voltage of the supercapacitor;

I_c — charging and discharging current of the supercapacitor.

3. DC Microgrid Control Optimization Model Based on P-U Sag

DC microgrids contain a large number of power electronic devices and are low-inertia systems. Under random power disturbances, voltage quality deteriorates significantly, leading to extensive research on virtual inertia control. However, DC microgrids under virtual inertia control generally suffer from stability issues. Therefore, this paper proposes a control optimization model for DC microgrids based on P-U droop control, aiming to optimize DC microgrid control and enhance system stability.

3.1. Small-Signal Modeling of DC Microgrids

This section will establish small-signal models for various converters, including large grid-side converters and wind turbine-side converters [33].

3.1.1. Small-Signal Model of Converters on the Large Grid Side

Voltage-type PWM converters are based on voltage-space vector pulse width modulation (SVPWM) control technology and employ a dual-loop feedback control method for voltage and current. The inner-loop reference current is generated using droop control and additional virtual inertia control, which is then compared with the AC-side feedback current after coordinate transformation. The result is processed by a PI controller and used as the reference value for the space vector to control the power switches. Based on the converter structure and control strategy, by aligning the grid voltage direction with the d-axis of the synchronous rotating coordinate system, the following system of differential equations in the d-q coordinate system can be derived:

$$\begin{cases} L_{cd}\dfrac{di_{cd}}{dt} = -R_c i_{cd} - k_1(M_{cdI} + M_{cdP})U_{dc} + U_e + \omega L_{cq} i_{cq} \\ L_{cq}\dfrac{di_{cq}}{dt} = -R_c i_{cq} - k_1(M_{cqI} + M_{cqP})U_{dc} - \omega L_{cd} i_{cd} \\ \dfrac{dM_{cdI}}{dt} = k_{cd_I}\{(U_{dcG} - U_{dc})/k_G - i_{cd} - C_{\text{var}G}/(2TU_{dc}) \times [(U_{deN}^2 - U_{dc}^2) - \delta U_{dc}/T]\} \\ \dfrac{dM_{cqI}}{dt} = k_{cq_I}(0 - i_{cq}) \end{cases} \tag{9}$$

In the equation:

L_{cd}, L_{cq}, R_c — synchronous inductance and resistance in the $d-q$ coordinate system,

M_{cd}, M_{cq} — amplitude modulation coefficients in the $d-q$ coordinate system, $M_{cdI}, M_{cqI}, M_{cdP}, M_{cqP}$ are their integral and proportional components;

U_e — Constant power supply;

k_1 — the proportional coefficient of the converter, with a value of $\sqrt{3}/(2\sqrt{2})$,

U_{dcG} — the DC voltage reference value when the G-VSC participates in voltage-layer coordinated control;

k_G — droop coefficient.

By linearizing equation (9) near the steady-state value, the small-signal model of the converter on the large grid side can be obtained, as shown in equation (10):

$$\frac{d\Delta x_g}{dt} = A_g \Delta x_g + B_g \Delta u \tag{10}$$

In the formula:

$$\Delta x_g = [\Delta i_{cd}, \Delta i_{cq}, \Delta M_{cdI}, \Delta M_{cqI}]^T \tag{11}$$

$$\Delta u = [\Delta U_{dc}, \Delta \delta U_{dc}]^T \tag{12}$$

$$A_g = \begin{bmatrix} -\frac{R_c - k_1 k_{cd\_p} U_{dc0}}{L_{cd}} & -\frac{\omega_0 L_{cd}}{L_{cq}} & -k_{cd\_I} & 0 \\ \frac{\omega_0 L_{cq}}{L_{cd}} & -\frac{R_c - k_1 k_{cq_P} U_{dc0}}{L_{cq}} & 0 & -k_{cq\_I} \\ -\frac{k_1 U_{dc0}}{L_{cd}} & 0 & 0 & 0 \\ 0 & -\frac{k_1 U_{dc0}}{L_{cq}} & 0 & 0 \end{bmatrix}^T \tag{13}$$

$$B_g = \begin{bmatrix} -\frac{k_1 M_{cd0}}{L_{cd}} + \frac{k_1 k_{cd_P} U_{dc0}}{L_{cd} k_G} + \frac{k_1 k_{cd_P} C_{virG} \alpha}{2TL_{cd} U_{dc\,0}} & -\frac{k_1 k_{cd_P} C_{virG}}{2T^2 L_{cd}} \\ -\frac{k_1 M_{cq0}}{L_{cq}} & 0 \\ -\frac{k_{cd_I}}{k_G} - \frac{k_{cd_I} C_{virG} \alpha}{2TU_{dc0}^2} & \frac{k_{cd_I} C_{virG}}{2T^2 U_{dc0}} \\ 0 & 0 \end{bmatrix} \tag{14}$$

3.1.2. Small-Signal Model of Wind Turbine Converter

Wind turbine generators also use voltage-type PWM converters to connect to DC microgrids, with the outer loop using maximum power tracking or simulated inertial control to capture maximum wind energy. The equivalent circuit of the PMSG, which is oriented by the rotor magnetic flux, and the converter control strategy can be obtained from the system of simultaneous differential equations in the d and q coordinates:

$$\begin{cases} L_{sd} \dfrac{di_{sd}}{dt} = -R_s i_{sd} + k_2 (M_{sdl} + M_{sdp}) U_{dc} + \omega_i L_{sq} i_{sq} \\ L_{sq} \dfrac{di_{sq}}{dt} = -R_s i_{sq} + k_2 (M_{sql} + M_{sqp}) U_{dc} - \omega_i L_{sd} i_{sd} - \omega_i \psi_f \\ \dfrac{dM_{sdl}}{dt} = k_{sd\_1} (0 - i_{sd}) \\ \dfrac{dM_{sql}}{dt} = k_{sq\_1} (-k_{vac} \omega_i^2 / \psi_f - i_{sq}) \end{cases} \tag{15}$$

In the equation:

L_{sd}, L_{sq}, R_s — synchronous inductance and resistance in the $d-q$ coordinate system;

M_{sd}, M_{sq} — amplitude modulation coefficients in the $d-q$ coordinate system, where $M_{sdI}, M_{sqI}, M_{sqP}$ are their integral and proportional components;

Ψ_f — constant flux of the PMSG, given by:

k_2 — proportional coefficient of the converter, with a value of $\sqrt{3}/(2\sqrt{2})$;

k_{vic} — virtual inertia control coefficient of the wind turbine, which can be further expressed in the small-signal model as:

$$k_{vic} = \frac{k_{opt}\omega_{r0}^3}{\{\omega_{r0}^2 - \frac{C_{virW}}{2H}[(U_{dcN}^2 - U_{dc}^2) - \delta U_{dc}/T]\}^{\frac{3}{2}}} \tag{16}$$

By linearizing Equation (15) near the steady-state value, we can obtain the small-signal model of the wind turbine converter, as shown in Equation (17):

$$\frac{d\Delta x_w}{dt} = A_w \Delta x_w + B_w \Delta u \tag{17}$$

In the formula:

$$\Delta x_w = [\Delta i_{sd}, \Delta i_{sq}, \Delta M_{sdI}, \Delta M_{sqI}]^T \tag{18}$$

$$A_w = \begin{bmatrix} -\frac{R_5 + k_2 k_{sd\_P} U_{de0}}{L_{sd}} & -\frac{\omega_{r0} L_{sd}}{L_{sq}} & -k_{sd\_I} & 0 \\ \frac{\omega_{r0} L_{sq}}{L_{sd}} & -\frac{R_s + k_2 k_{sq\_P} U_{de0}}{L_{sq}} & 0 & -k_{sq\_I} \\ \frac{k_2 U_{de0}}{L_{sd}} & 0 & 0 & 0 \\ 0 & \frac{k_2 U_{de0}}{L_{sq}} & 0 & 0 \end{bmatrix}^T \tag{19}$$

$$B_w = \begin{bmatrix} \frac{k_2 M_{sd0}}{L_{sd}} & 0 \\ \frac{k_2 M_{sq0}}{L_{sq}} + \frac{\gamma k_2 C_{virW} k_{sq_P} U_{dc0}^2}{L_{sq}\beta} & \frac{\gamma k_2 C_{virW} k_{sq_P} U_{dc0}}{2TL_{sq}\beta} \\ 0 & 0 \\ \frac{\gamma C_{virW} k_{sq_1} U_{dc0}}{\beta} & \frac{\gamma C_{virW} k_{sq\_I}}{2T\beta} \end{bmatrix} \tag{20}$$

3.1.3. Small-Signal Model of Battery-Side Converter

The reference current for sag control and additional virtual inertia control output is compared with the feedback current on the battery side. After passing through a PI controller, the duty cycle is adjusted to control the power switch. The system of coupled differential equations is as follows:

$$\begin{cases} L_b \frac{di_b}{dt} = U_b - (1 - g_1) U_{dc} \\ \frac{dg_{II}}{dt} = k_{b_I} \{(U_{dcB} - U_{dc})/k_B - i_b - C_{vinB}/(2TU_{dc}) \times [(U_{dcN}^2 - U_{dc}^2) - \delta U_{dc}/T]\} \end{cases} \tag{21}$$

In the equation:

g_1 — Duty cycle during B-DC discharge, where g_{1I}, g_{1P} are its integral and proportional components;

U_{dcB} — DC voltage reference value when B-DC participates in voltage stratification coordination control;

k_B — Sag coefficient;

By linearizing equation (21) near the steady-state value, the small-signal model of the battery converter can be obtained, as shown in equation (22):

$$\frac{d\Delta x_b}{dt} = A_b \Delta x_b + B_b \Delta u \tag{22}$$

Equation $\Delta x_b = [\Delta i_b, \Delta g_{1I}]^T$:

$$A_b = \begin{bmatrix} -\dfrac{k_{b_P} U_{dc0}}{L_b} & -k_{b_I} \\ \dfrac{U_{dc0}}{L_b} & 0 \end{bmatrix}^T \tag{23}$$

$$B_b = \begin{bmatrix} \dfrac{g_{10}-1}{L_b} - \dfrac{k_{b\_B} U_{dc0}}{L_b k_B} - \dfrac{k_{b\_P} C_{virB} \alpha}{2TL_b U_{dc0}} & \dfrac{k_{b\_P} C_{virB}}{2T^2 L_b} \\ -\dfrac{k_{b\_I}}{k_B} - \dfrac{k_{b\_I} C_{virB} \alpha}{2TU_{dc0}^2} & \dfrac{k_{b\_I} C_{virB}}{2T^2 U_{dc0}} \end{bmatrix} \tag{24}$$

3.1.4. Small-Signal Model of DC Microgrid Systems

In a DC microgrid, the output currents of all units are collected on the DC bus.

Based on the KCL relationship of the network, the differential equation for the DC bus voltage can be written as:

$$C_{dc} \frac{dU_{dc}}{dt} = I_{wind} + I_{pv} + I_{grid} + I_{bat} - I_{Load} \tag{25}$$

In the formula:

1) $I_{wind} = 3(M_{sd} i_{sd} + M_{sq} i_{sq})/2$;

2) $I_{gnid} = 3(M_{cd} i_{cd} + M_{cq} i_{cq})/2$;

3) $I_{bat} = (1-g_1) i_b$;

4) $I_{pv} = P_{pv} / U_{dc}$;

5) $I_{Load} = P_{Load} / U_{dc}$.

In the virtual inertia control of each converter, a first-order inertia element is introduced. The inertia voltage input δU_{dc} after passing through this element is used to control the inertia power output. The differential equation of δU_{dc} is:

$$\frac{d\delta U_{dc}}{dt} = (U_{dcN}^2 - U_{dc}^2) - \delta U_{dc} / T \tag{26}$$

Treat U_{dc} and δU_{dc} as state variables and perform linearization to obtain the small-signal model of the DC microgrid:

$$\frac{d\Delta x}{dt} = A_{sys} \Delta x \tag{27}$$

In the formula:

$\Delta x = [\Delta x_g \Delta x_w \Delta x_b \Delta u]^T$,

$A_{595} = \begin{bmatrix} A_5 & 0 & 0 & B_5 \\ 0 & A_w & 0 & B_w \\ 0 & 0 & A_b & B_b \\ A_{g0} & A_{w0} & A_{b0} & A_{dl} \end{bmatrix}$. The matrix elements $A_{g0} A_{w0} A_{b0} A_{d1}$ are as follows:

$$1)\ A_{g0}=\begin{bmatrix}\frac{3(M_{cd0}-k_{cd\_P}i_{cd0})}{2C_{dc}} & \frac{3(M_{cq0}-k_{cq\_P}i_{cq0})}{2C_{dc}} & \frac{3i_{cd0}}{2C_{dc}} & \frac{3i_{cq0}}{2C_{dc}}\\ 0 & 0 & 0 & 0\end{bmatrix};$$

$$2)\ A_{w0}=\begin{bmatrix}\frac{3(M_{sd0}-k_{sd\_P}i_{sd0})}{2C_{dc}} & \frac{3(M_{sq0}-k_{sq\_P}i_{sq0})}{2C_{dc}} & \frac{3i_{sd0}}{2C_{dc}} & \frac{3i_{sq0}}{2C_{dc}}\\ 0 & 0 & 0 & 0\end{bmatrix};$$

$$3)\ A_{b0}=\begin{bmatrix}\frac{1-g_{10}+k_{b\_P}i_{b0}}{C_{dc}} & -\frac{i_{b0}}{C_{dc}}\\ 0 & 0\end{bmatrix};$$

$$4)\ A_{d1}=\begin{bmatrix}A_{d10} & A_{d11}\\ -2U_{dc0} & -\frac{1}{T}\end{bmatrix}.$$

The $\alpha,\beta,\gamma,A_{d10},A_{d11}$ appearing in the matrix are:

$$1)\ \alpha=\delta U_{dc0}/T-U_{dc0}^2-U_{dcN}^2;$$

$$2)\ \beta=2H\psi_f[\omega_{r0}^2-C_{virW}(U_{dcN}^2-U_{dc0}^2-\delta U_{dc0}/T)/2H]^{\frac{5}{2}};$$

$$3)\ \gamma=3k_{opt}\omega_{r0}^5;$$

4)

$$-A_{d10}=\frac{3\gamma C_{virW}k_{sq\_P}U_{dc0}i_{sq0}}{2C_{dc}\beta}+\frac{3k_{cd\_P}i_{cd0}}{2C_{dc}}(-\frac{1}{k_G}-\frac{C_{virG}c\chi}{2TU_{dc0}^2})+\frac{k_{b\_P}i_{b0}}{C_{dc}}(\frac{1}{k_B}+\frac{C_{virB}c\chi}{2TU_{dc0}^2})-\frac{P_{pv}}{C_{dc}U_{dc0}^2}+\frac{P_{Load}}{C_{dc}U_{dc0}^2}$$

;

$$5)\ A_{d11}=\frac{3\gamma C_{virW}k_{sq\_P}i_{sq0}}{4TC_{dc}\beta}+\frac{3k_{cd\_P}C_{virG}i_{cd0}}{4T^2C_{dc}U_{dc0}}-\frac{k_{b\_P}C_{virB}i_{b0}}{2T^2C_{dc}U_{dc0}}.$$

3.2. AVDCM Control Considering Power Coordination Allocation

The dual-closed-loop P-U droop control of the bidirectional DC/DC converter in the energy storage interface can basically maintain the stability of the bus voltage and the balance of power distribution, but it does not have inertia characteristics and damping characteristics, and its dynamic characteristics are poor. When encountering sudden changes in load power, its ability to regulate voltage is poor. To address this issue, this paper considers improving its dynamic characteristics from two aspects.

3.2.1. Traditional Sag Control

In a DC microgrid, the DC bus connects almost all devices, and its voltage is the most critical parameter in the DC microgrid. Therefore, control of the DC microgrid is typically performed based on the bus voltage. The droop control of the energy storage interface in a DC microgrid is divided into U-I droop control and P-U droop control. U-I droop control reflects power conditions through the magnitude and direction of current, meaning that when battery discharge is required, the current is positive, and negative when charging is required. P-U droop control directly measures power parameters and balances power output through droop curve correction. This paper adopts P-U droop control as the control method for multi-energy storage interface converters [34].

U_{bat1},U_{bat2} ——Output voltage of the two energy storage devices/(V)

I_1,I_2 ——Output current of the interface converters of the two energy storage devices/(A);

$U_{bus\_ref1},U_{bus\_ref2}$ Output voltage of the interface converters of the two energy storage devices/(V);

R_{line1},R_{line2} — the sum of the internal resistance of the interface converters of the two energy storage devices and the impedance of the cables (Ω);

R_1, R_2 — virtual impedance (droop coefficient) (Ω).

Then, the proportional relationship between the output currents of the interface converters of the two energy storage devices is:

$$\frac{I_1}{I_2} = \frac{R_2 + R_{line2}}{R_1 + R_{line1}} \tag{28}$$

As can be seen from Equation (28), the magnitude of the output current of each energy storage interface converter is inversely proportional to the virtual impedance and cable impedance. In this equation, the line impedance R_{line} is constant, while the virtual impedance R is variable. Therefore, by adjusting the value of the virtual impedance, the output current of each energy storage device can be altered, thereby modifying the output power. However, to reduce the influence of the line impedance R_{line}, the value of the virtual impedance R should be set much larger than the line impedance R_{line} to reduce the current sharing of R_{line} and improve control accuracy. In PU droop control, the larger the virtual impedance introduced, the smaller the influence of the converter's internal resistance and the line impedance on power balancing.

U_{o_H}, U_{o_L} represent the upper and lower limits of the DC bus voltage operation, respectively, U_N is the output voltage of the energy storage device under normal conditions, and U_{bus_ref} is the reference bus voltage of the energy storage interface converter after droop control. $P_{bat\_\max}$ and $P_{bat\_\min}$ represent the maximum output power and minimum absorption power of the energy storage device, respectively.

The formula for P-U droop control is derived as follows:

$$U_{bus\_ref} = U_N - kP_o \tag{29}$$

In the formula:

U_{bus_ref} — Set value of energy storage converter output voltage/(V);

U_N — Rated value of DC bus voltage/(V);

k — Sag coefficient.

The sag coefficient is equivalent to the reciprocal of the virtual impedance, i.e., 1/R, and its expression is:

$$k = \frac{1}{R} = \frac{U_{oH} - U_{oL}}{P_{bat\_\max} - P_{bat\_\min}} \tag{30}$$

The output power P of the energy storage interface converter is derived from equation (30) as follows:

$$P_{om} = \frac{U_N - U_{bus\_ref}}{k_m} \tag{31}$$

In the formula:

P_{om} — Output power of the mth energy storage converter (W);

k_m — Droop coefficient of the mth energy storage converter.

In addition, the droop control of the energy storage interface converter has upper and lower limits, indicating the maximum power operating state of the energy storage unit. If the power exceeds the limits, the energy storage unit can only maintain the maximum power state. Therefore, it is necessary to use multiple energy storage units to provide voltage support for the DC microgrid.

3.2.2. Improving Sag Control

In P-U droop control, the droop coefficient is $1/R$, which makes the output power P_o of the bidirectional DC/DC converter linearly proportional to the voltage. When the power changes abruptly, the voltage changes accordingly, resulting in poor disturbance immunity. Therefore, we consider optimizing the P-U droop control by introducing a first-order differential element into the P-U droop control equation. The differential element reduces voltage fluctuations during load power fluctuations, lowering the amplitude of voltage fluctuations without affecting control stability.

The improved P-U droop control equation is:

$$U_{bus\_ref} = U_N - \frac{1}{sL+R} P_o \tag{32}$$

In the formula:

L — virtual inductance (differential coefficient) / (mH);

R — virtual resistance / (Ω).

The improved P-U droop control block diagram is shown in Figure 2:

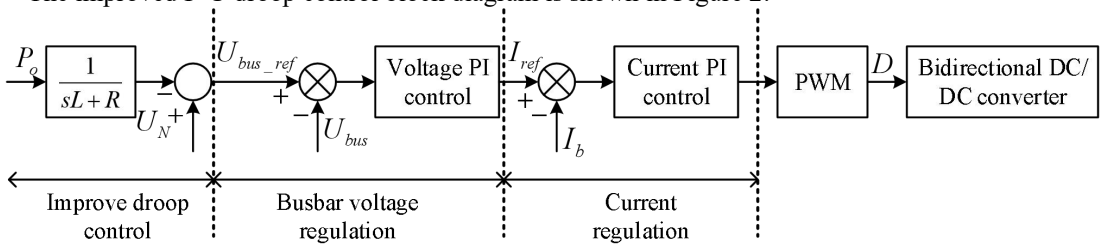

Figure 2. Block diagram of the improved P-U droop control.

After improving the double closed-loop P-U droop control of the bidirectional DC/DC converter for energy storage interfaces, a differential element was added. The leading control of this element can improve the dynamic stability of the system, enhance the dynamic regulation capability of the DC microgrid during sudden changes in bus voltage, and improve the dynamic stability of the DC microgrid.

3.2.3. VDCM Control Based on Improved P-U Sag Coordination

In order to further improve the overall control effect, the improved P-U droop control and VDCM control are combined to form a VDCM control based on the improved P-U droop coordination (hereinafter referred to as the improved P-U droop VDCM control), which provides inertia characteristics and damping characteristics for the system. This method can take into account the problem of power distribution and the dynamic stability of bus voltage at the same time.

First, verify the stability of the control method by constructing a small-signal model of a virtual DC motor based on P-U droop coordination, where the transfer function of the improved droop control is:

$$G_{XC}(s) = \frac{1}{sL+R} \tag{33}$$

Then, the open-loop transfer function controlled by P-U droop VDCM is:

$$G_{up}(s) = \frac{\Delta u_{bus}}{\Delta p_o} = \frac{G_{XC}(s)G_{PI1}(s)G_V(s)G_P(s)G_{PI2}(s)G_m(s)G_{ud}(s)}{1+G_{PI2}(s)G_m(s)G_{id}(s)+G_P(s)G_{PI2}(s)G_m(s)G_{ud}(s)} \tag{34}$$

Plot the open-loop Nyquist plot and Bode plot using $G_{up}(s)$ to verify the effect of parameter L changes in the improved droop control on the stability of the DC microgrid.

3.2.4. AVDCM Control Based on Improved P-U Droop Coordination

Changes in light intensity directly affect the output power of photovoltaic systems. If the output power of the photovoltaic system cannot meet the load demand, energy storage output power is required to balance the system. To avoid mutual interference between the output power of the photovoltaic system and the input power of the droop control, fuzzy control is set as a single input, i.e., only the rate of change of bus voltage is used as the input for fuzzy control, and the rotational inertia J is used as the output of fuzzy control.

After incorporating droop control, the stable bus voltage is no longer 400 V but fluctuates around 400 V. Therefore, the domains and membership functions for the rate of change of bus voltage and rotational inertia J in the fuzzy control must be redefined. The domain of the bus voltage in the new fuzzy control is set to $dU_{bus}/dt \in (-10V/s, 10V/s)$, and the absolute value is taken in the simulation, i.e., $|dU_{bus}/dt| \in (0, 10V/s)$. The corresponding fuzzy subsets are represented as $\{a,b,c,d,e,f\}$, representing the bus voltage change rate as "close to zero," "small," "slightly small," "medium," "slightly large," and "large," respectively. The fuzzy input is preceded by a triangular membership function to improve its sensitivity and better distinguish smaller voltage changes, followed by a trapezoidal function to treat larger portions of the voltage change rate as a whole, to avoid continuous changes in the output inertia. The domain of the rotational inertia J is set to $J \in (0.1, 6.5)$, with the corresponding fuzzy subsets being $\{F,E,D,C,B,A\}$, representing the rotational inertia J as

"minimum," "small," "slightly small," "medium," "slightly large," and "maximum," respectively. The fuzzy output is triangular at the front, outputting a smaller J corresponding to a larger range of voltage change rates in the fuzzy input, and trapezoidal at the back, corresponding to smaller voltage change rates in the fuzzy input, outputting a larger and more stable J.

4. DC microgrid Stability Simulation Experiment

To verify the stability improvement performance of the DC microgrid control optimization model based on P-U sag constructed in this paper, this chapter will conduct DC microgrid stability simulation experiments using a DC microgrid with virtual inertia control as a comparison object.

4.1. Experimental Parameters

In Simulink, a simulation model of a DC microgrid is constructed, with all loads set as constant power loads. The component parameters of the DC microgrid are specified as shown in Table 1. The rated capacity of the grid-connected converter is 30 kW. The filter inductor, inductor resistance, and DC bus capacitor are set to 0.00032 L/H, 0.00073 R/Ω, and 0.041 C/F, respectively. The droop coefficient k is set to 0.0666.

Table 1. DC microgrid system parameters.

Parameters	Numerical value
Filter inductance (L/H)	0.00032
Inductor resistance (R/Ω)	0.00073
DC bus capacitor (C/F)	0.041
Droop coefficient k	0.0666
PI controller proportional integral coefficient k_p, k_i	1, 50
Time constant T	0.05

4.2. Analysis of Experimental Results

The initial load power is 5 kW, and an additional 5 kW is added at 10 s. The simulation of the DC microgrid system with additional virtual inertia control at C_{vir} = 0, 10, and 21 is shown in Figure 3. By comparing the dynamic response curves of the DC bus voltage under the three conditions, it can be seen that the additional virtual inertia control exhibits good performance in suppressing sudden changes in the DC bus voltage. The larger the virtual inertia coefficient, the greater the system inertia. When C_{vir} = 10, the system can still maintain stable operation. However, when C_{vir} = 21, the source-side impedance Z_o and the load-side impedance Z_L have equal magnitudes but differ in phase by 180°, resulting in high-frequency harmonics. A high-frequency oscillation component is superimposed on the DC bus voltage, causing the system to become unstable.

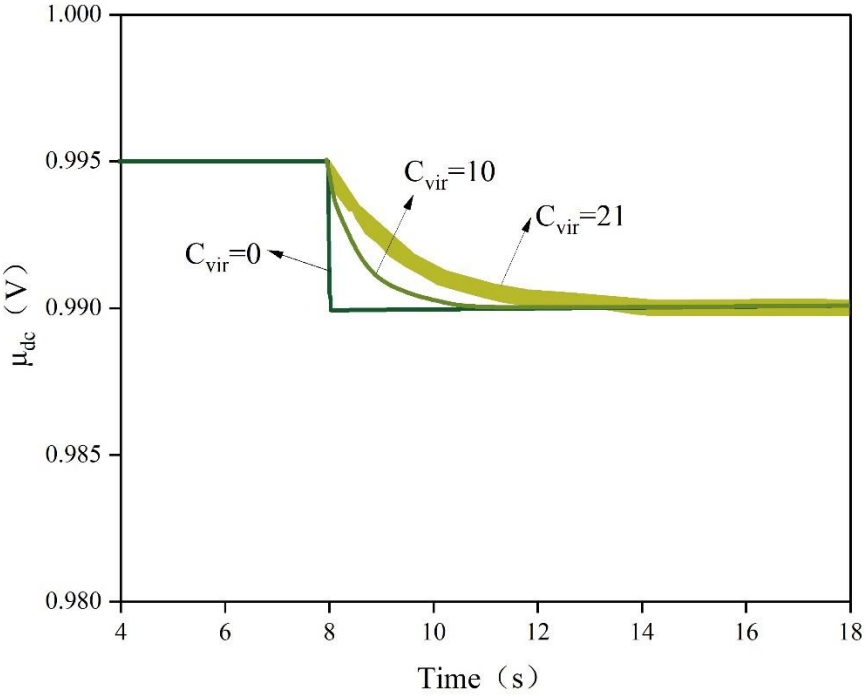

Figure 3. DC micro-grid system with virtual inertia control.

When only P-U droop coordination control is applied, the simulation diagram of the DC microgrid system is shown in Figure 4. The DC bus voltage changes with the increase in load power. The initial load is 5 kW, and 5 kW is added at 5 s, 10 s, 15 s, and 20 s, and another 5 kW is added at 30 s. The system can operate stably under all these conditions.

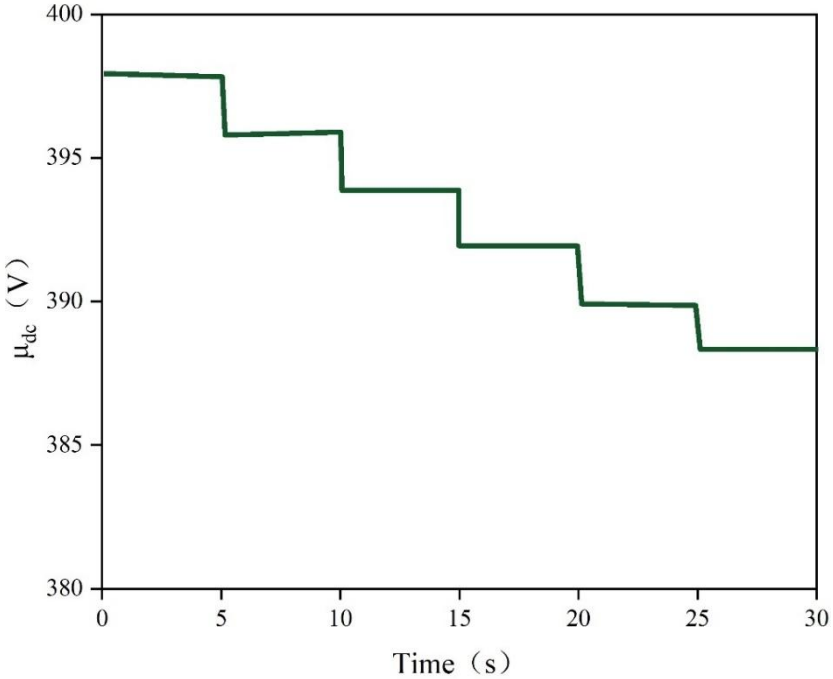

Figure 4. DC microgrid system based on P-U droop coordinated control.

When C_{vir} = 16, the load power changes as described above. The simulation of the DC microgrid system with virtual inertia control is shown in Figure 5. As shown in the figure, after a 5 kW load increase at 5 seconds, the system exhibited minor oscillations, but the amplitude decayed and quickly returned to a stable state. At 10 seconds, when the load increased to 15 kW, due to the interaction between the source-side impedance Z_o and the load-side impedance Z_L, the DC microgrid system experienced high-frequency oscillations. It can be observed that there is a slight fluctuation in load power when it increases to 10 kW, and after increasing to 15 kW, the system undergoes oscillations, with the amplitude

of u_{dc} reaching its maximum at 20 kW.

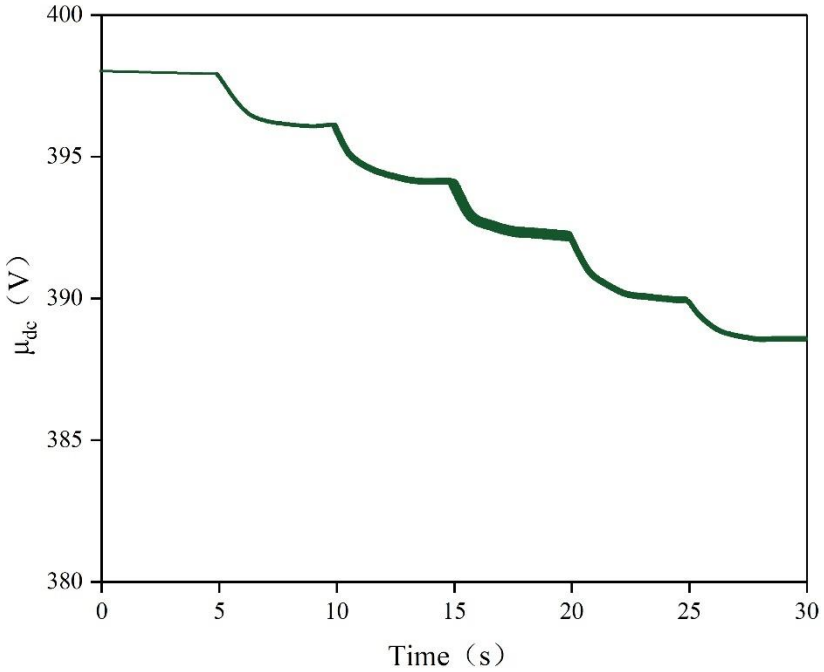

Figure 5. Simulation of virtual inertial control system.

Compared with the P-U droop coordinated control proposed in this paper, it can be seen that although virtual inertia control can enhance the inertia of the system and improve voltage quality, it weakens the stability of the system, and the oscillation amplitude changes with the constant power load power. The P-U droop coordinated control method proposed in this paper can make the DC microgrid more stable.

5. DC Microgrid Control Optimization Simulation Experiment

This chapter will simulate various disturbances that may occur in the operation of a DC microgrid system based on two operating modes: grid-connected and islanded. It will explore the control optimization effects of the P-U droop-based DC microgrid control optimization model proposed in this paper. The DC microgrid simulation model established in this chapter adopts a widely used radial busbar structure.

5.1. Simulation Verification under Grid-Connected Operation

Under initial conditions, the battery banks P_{load1} and P_{load2} are set to 95 kW and 5 kW, respectively, such that P_{load} equals 100 kW. The photovoltaic panels operate under conditions of 800 W/m² irradiance and 25°C temperature. At 0.5 seconds, P_{load1} suddenly changes to 155 kW, and at 0.7 seconds, the irradiance of the photovoltaic panels is increased from 800 W/m² to 1000 W/m². The simulation waveforms of the output power of the photovoltaic power source and the output current of the battery under grid-connected operation are shown in Figure 6. Figures (a) and (b) correspond to the output power of the photovoltaic power source and the output current of the battery, respectively. Before 0.6 seconds, the power of the photovoltaic power source remains almost stable at the maximum output power under standard conditions. After 0.6 seconds, the increase in light intensity causes the output power of the photovoltaic panels to increase to 1.2 times the original value. This indicates that the control of the model in this paper has achieved the expected objectives, and the charging current of the battery is maintained at around 48 A.

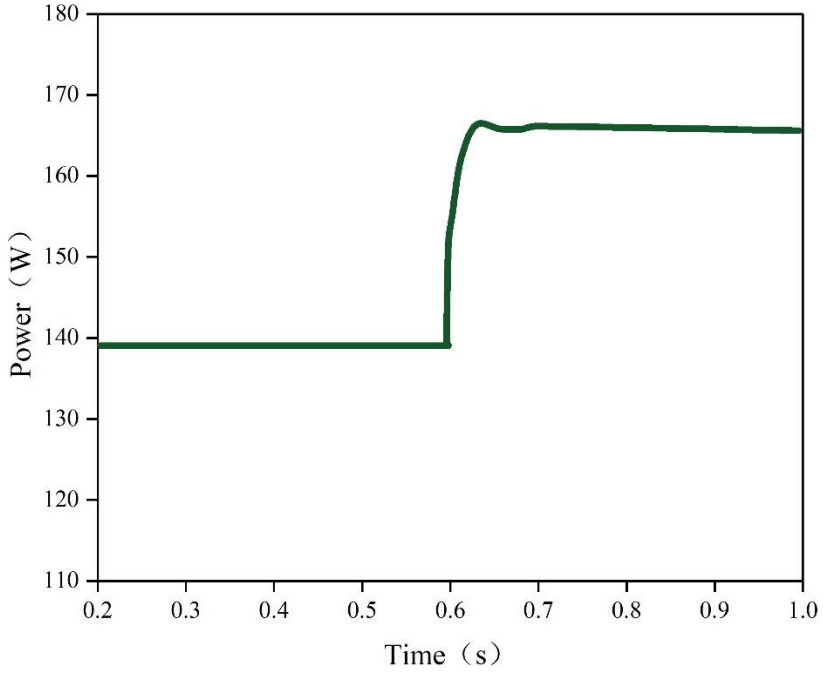

(a)Output power of photovoltaic power supply

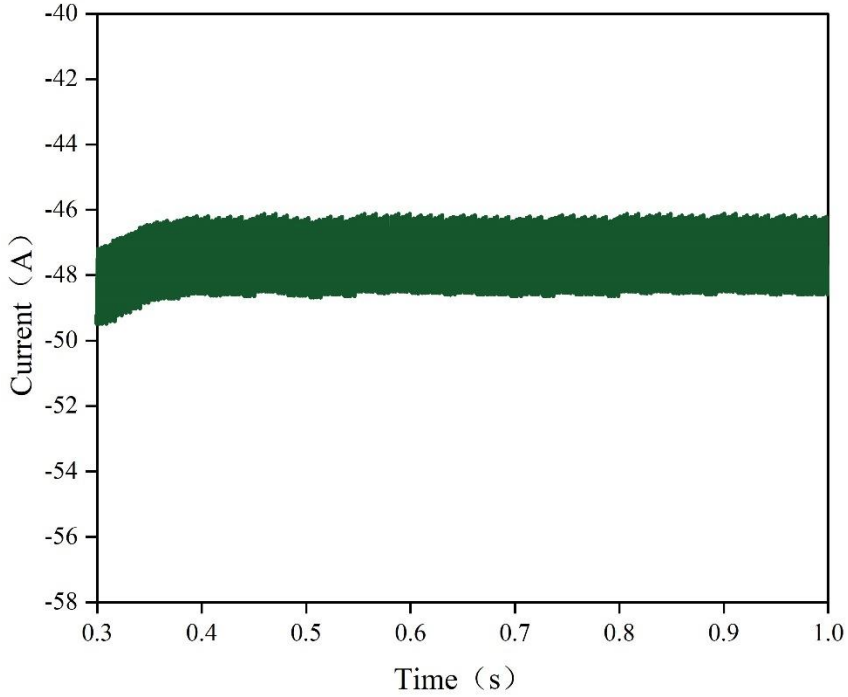

(b)Output current of the battery

Figure 6. Output power of PV and output current of battery in grid-connected mode.

The power exchange of the grid-connected converter under grid-connected operation is shown in Figure 7. It can be seen that at the beginning, the DC microgrid supplies power to the AC distribution network. Due to a sudden change in load at 0.5 s, P_{line} changes from a negative value to a positive value, i.e., the AC distribution network supplies power to the DC microgrid. Subsequently, the increase in the power of the photovoltaic panels stabilises P_{line} at around 5 kW, basically maintaining power balance.

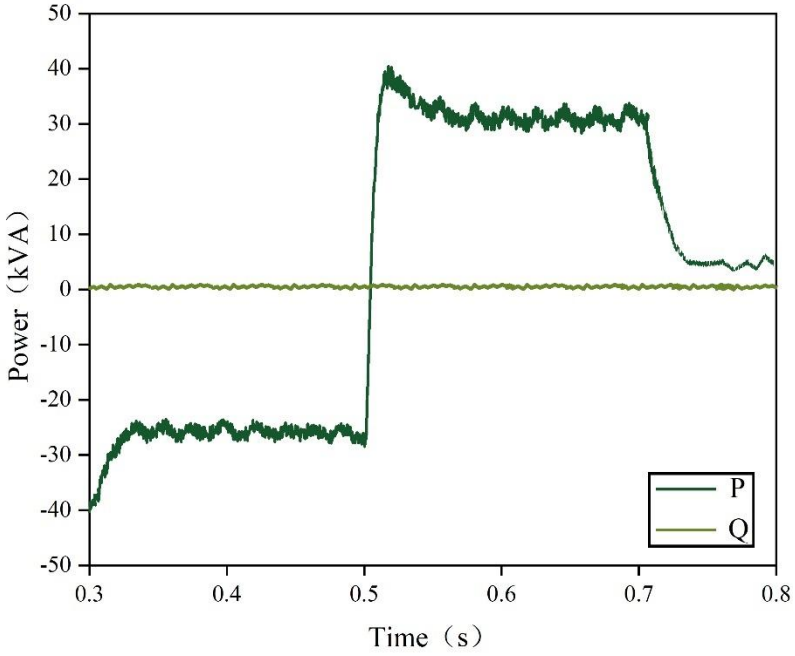

Figure 7. Switching power of AC/DC converter in grid-connected mode.

The specific conditions of the 700V DC bus voltage and 48V DC bus voltage under grid-connected operation are shown in Figure 8. Figures (a) and (b) correspond to the 700V DC bus voltage and 48V DC bus voltage, respectively. At 0.5 seconds, the sudden increase in power demand caused the 700V DC bus voltage to temporarily drop below 698V, but it quickly recovered to normal levels. At 0.7 seconds, the increased power output from the photovoltaic panels due to changes in sunlight caused the 700V DC bus voltage to rise to nearly 702V, and it also recovered to 700V within 0.1 seconds. The DC microgrid control optimization model proposed in this paper, based on P-U droop, can maintain the DC bus voltage at a constant state.

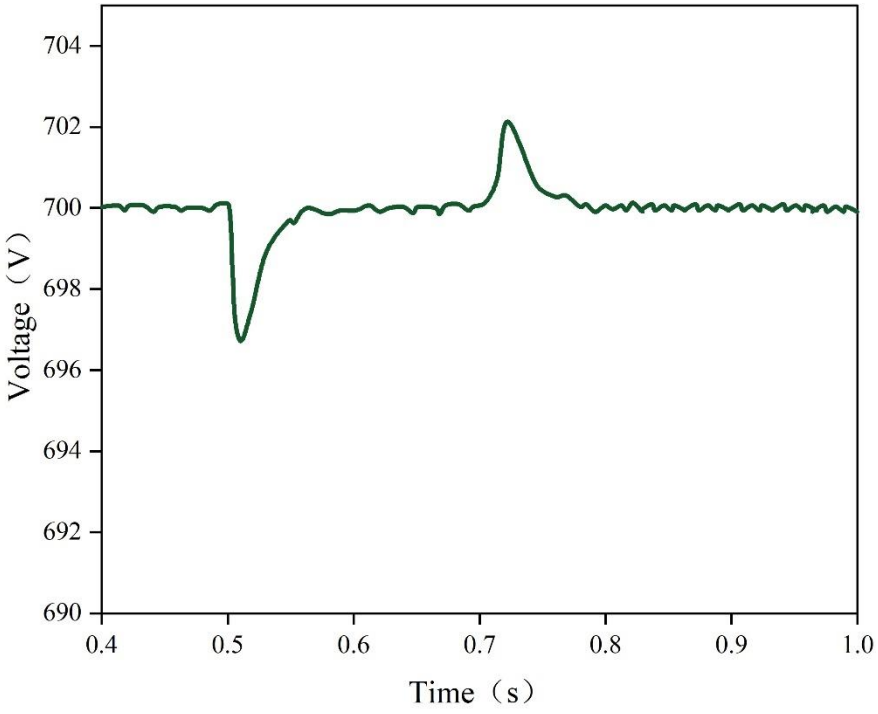

(a)700V DC bus voltage

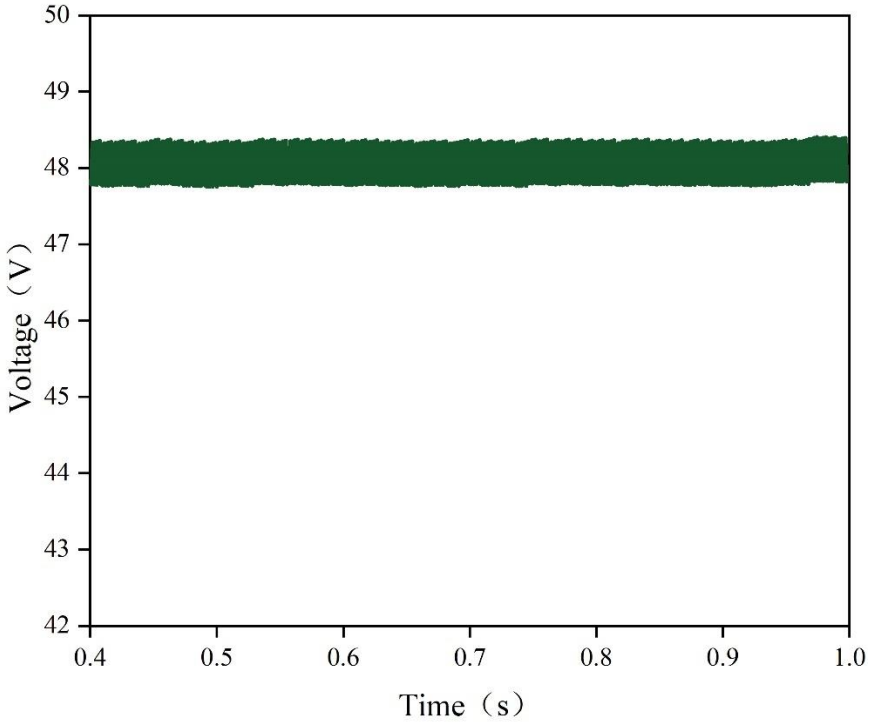

(b)48V DC bus voltage

Figure 8. 700V DC bus voltage and 48V DC bus voltage in grid-connected mode.

5.2. Simulation Verification under Isolated Island Operation

In islanded operation mode, the microgrid separator is in the disconnected state, so the power exchange between the DC bus and the AC distribution network is 0. The initial conditions are the same as those in grid-connected operation mode, with P_{load1} and P_{load2} set to 95 kW and 5 kW, respectively, i.e., P_{load} equals 100 kW. The photovoltaic panels operate under conditions of 1000 W/m² irradiance and 25°C temperature. At 0.5 s, P_{load1} suddenly changes to 155 kW, and at 0.7 s, the temperature of the photovoltaic panels drops from 25°C to 5°C.

The output power of the photovoltaic power source and the output current of the battery during islanded operation are shown in Figure 9. Figures (a) and (b) correspond to the output power of the photovoltaic power source and the output current of the battery, respectively. The battery is in charging mode. At 0.5 seconds, the sudden change in load causes the value of Pbat to change from positive to negative, and the battery switches from charging to discharging mode. During this process, there is a buffer phase where part of the output current is zero, indicating that the offline zone set in the improved droop control has a protective effect. Around 0.7 seconds, the decrease in the operating temperature of the photovoltaic panels causes the output power of the photovoltaic panels to rise to between 144 kW and 146 kW in a very short time, thereby reducing the power supply burden on the battery and causing its output current to drop slightly.

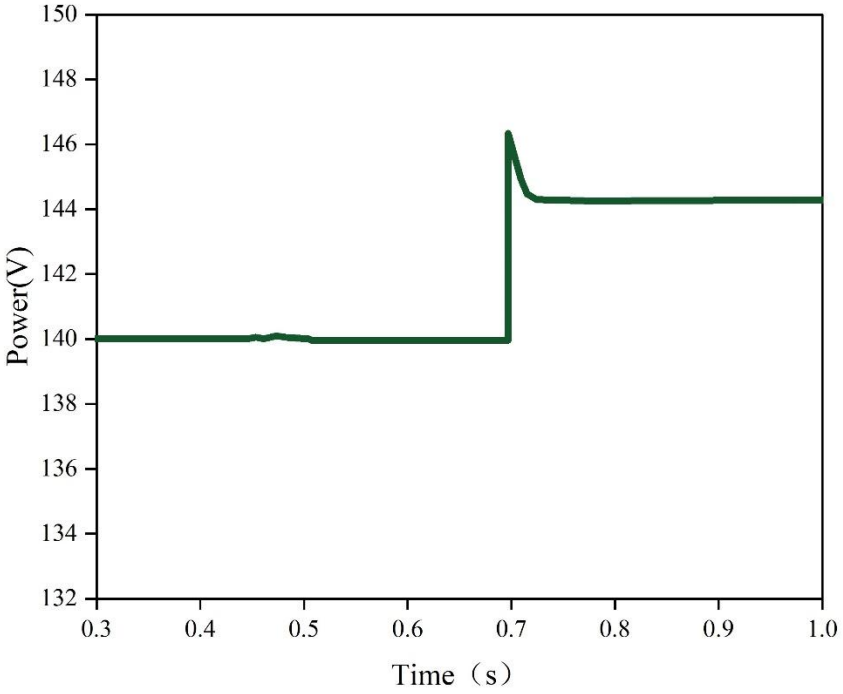

(a)Output power of PV

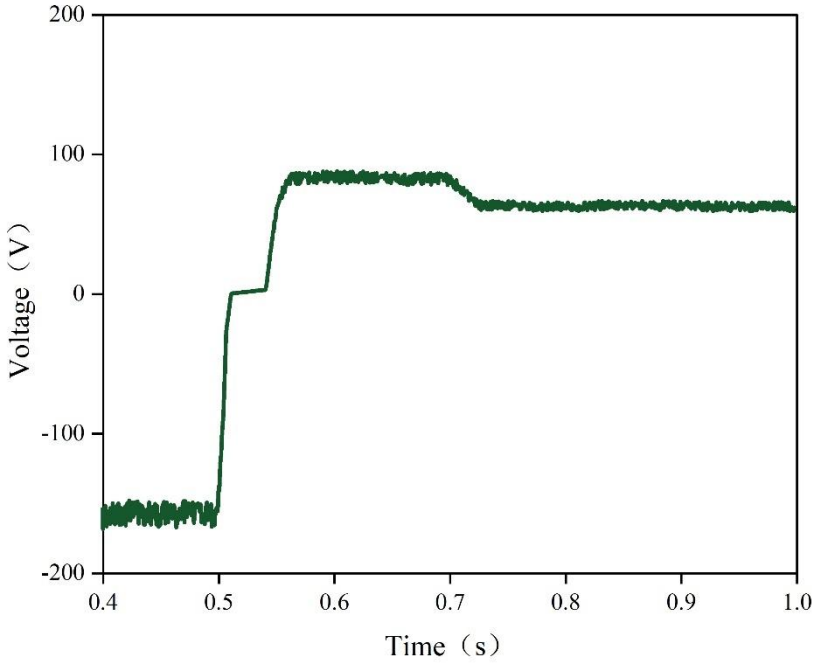

(b)Output current of battery

Figure 9. Output power of PV and output current of battery in island mode.

The specific values of the 700V DC bus voltage and 48V DC bus voltage under isolated island operation are shown in Figure 10. Figures (a) and (b) correspond to the 700V DC bus voltage and 48V DC bus voltage, respectively. Similarly, it can be observed that the 700V DC bus voltage exhibits voltage drops and recoveries during this process, with patterns consistent with the operating zones corresponding to different voltage ranges in P-U droop control. Therefore, the load can operate reliably, while the 48V DC bus voltage remains maintained at a constant state.

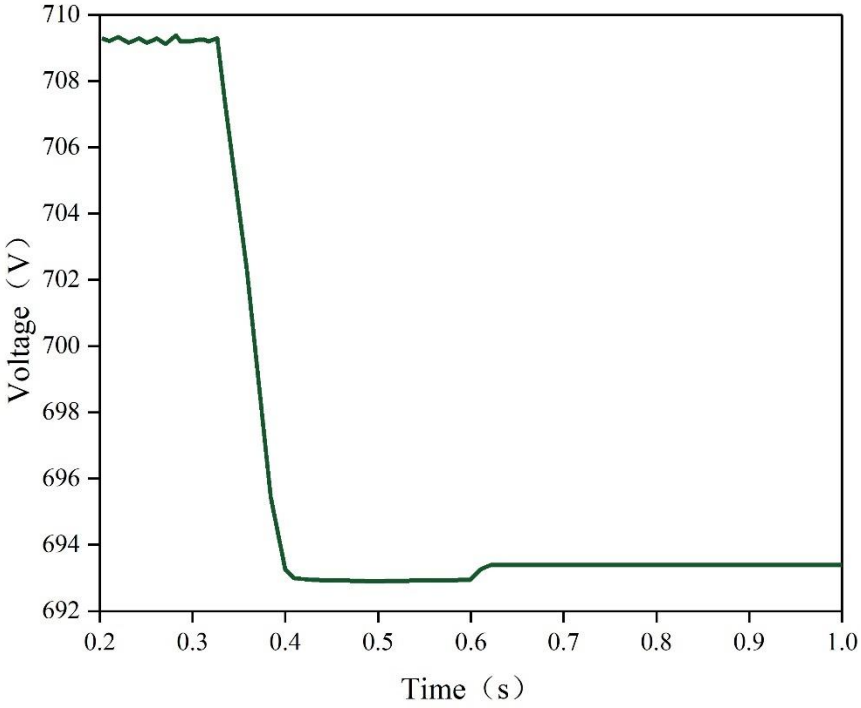

(a)700V DC bus voltage

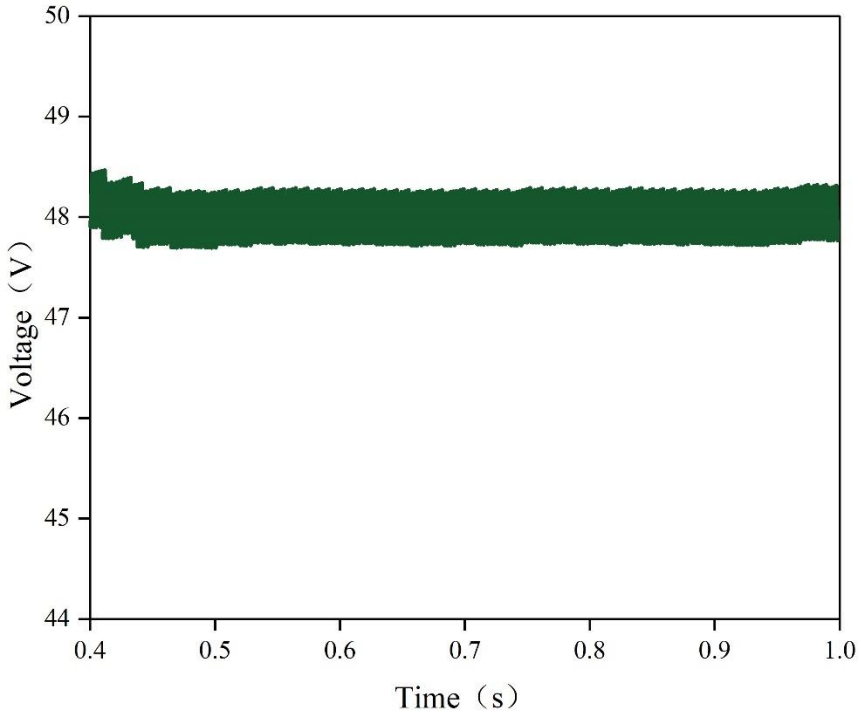

(b)48V DC bus voltage

Figure 10. 700V DC bus voltage and 48V DC bus voltage in island mode.

6 Conclusion

This paper constructs a mathematical model of a DC microgrid system and, based on this, introduces droop control into AVDCM control, proposing a control optimization model for DC microgrids based on P-U droop.

Using a DC microgrid with virtual inertia control as a reference, stability simulation experiments were conducted on the DC microgrid. Virtual inertia control demonstrated excellent performance in suppressing sudden changes in DC bus voltage, but when C_{vir} = 21, high-frequency harmonics appeared in the DC microgrid, causing the system to become unstable. When C_{vir} = 16, due to the interaction

between the source-side impedance Z_o and the load-side impedance Z_L, the DC microgrid system also experienced high-frequency oscillations. However, when only the P-U droop coordination control method proposed in this paper was used, the DC microgrid system could always operate stably and exhibited superior stability.

Starting from the two operating modes of grid-connected and islanded operation, we conducted simulation experiments on the control optimization of a DC microgrid system, simulating various disturbances that the DC microgrid system may encounter during operation. In grid-connected mode, the power output of the photovoltaic power source remains stable at the maximum output power under standard conditions for the first 0.6 seconds. After 0.6 seconds, the increase in light intensity causes the output power of the photovoltaic panels to rise to 1.2 times the original value, while the charging current of the battery remains around 48A. The control optimization performance of the model in this study aligns with expectations. The grid-connected converter's power exchange remains stable at around 5 kW, maintaining power balance. Both the 700 V DC bus voltage and the 48 V DC bus voltage exhibit minor fluctuations, but both quickly recover to normal levels within 0.1 seconds, with the DC bus voltage generally maintaining a constant state. In islanded operation mode, around 0.7 seconds, the decrease in photovoltaic panel operating temperature caused the output power of the photovoltaic panels to rise to between 144 kW and 146 kW in a very short time, thereby reducing the power supply burden on the batteries to some extent. The 700 V DC bus voltage exhibited voltage drops and recoveries, but these generally align with the operating zones corresponding to different voltage ranges in P-U droop control, ensuring reliable load operation. Meanwhile, the 48 V DC bus voltage remains at a constant state. The control optimization performance of the proposed P-U droop-based DC microgrid control optimization model is outstanding.

Funding

The research is supported by Liaoning Provincial Department of Education University Basic Research Projects (LJ242411632066).

References

1. Bouzid, A. M., Guerrero, J. M., Cheriti, A., Bouhamida, M., Sicard, P., & Benghanem, M. (2015). A survey on control of electric power distributed generation systems for microgrid applications. Renewable and Sustainable Energy Reviews, 44, 751-766.
2. Zhang, L., Gari, N., & Hmurcik, L. V. (2014). Energy management in a microgrid with distributed energy resources. Energy Conversion and Management, 78, 297-305.
3. Muhtadi, A., Pandit, D., Nguyen, N., & Mitra, J. (2021). Distributed energy resources based microgrid: Review of architecture, control, and reliability. IEEE Transactions on Industry Applications, 57(3), 2223-2235.
4. Lezhniuk, P., Hunko, I., Kravchuk, S., Komada, P., Gromaszek, K., Mussabekova, A., ... & Arman, A. (2017). The influence of distributed power sources on active power loss in the microgrid. Przeglad Elektrotechniczny, 93(3), 107-112.
5. Justo, J. J., Mwasilu, F., Lee, J., & Jung, J. W. (2013). AC-microgrids versus DC-microgrids with distributed energy resources: A review. Renewable and sustainable energy reviews, 24, 387-405.
6. Liu, G. (2019, September). Application of ETAP in distributed power supply and micro-grid interconnection. In 2019 4th International Conference on Intelligent Green Building and Smart Grid (IGBSG) (pp. 108-112). IEEE.
7. Yu, B., Guo, J., Zhou, C., Gan, Z., Yu, J., & Lu, F. (2017, May). A review on microgrid technology with distributed energy. In 2017 International Conference on Smart Grid and Electrical Automation (ICSGEA) (pp. 143-146). IEEE.
8. Palizban, O., & Kauhaniemi, K. (2015). Hierarchical control structure in microgrids with distributed generation: Island and grid-connected mode. Renewable and Sustainable Energy Reviews, 44, 797-813.
9. Li, X., Guo, L., Li, Y., Guo, Z., Hong, C., Zhang, Y., & Wang, C. (2017). A unified control for the DC–AC interlinking converters in hybrid AC/DC microgrids. IEEE Transactions on Smart Grid, 9(6), 6540-6553.
10. Kumar, M., Srivastava, S. C., & Singh, S. N. (2015). Control strategies of a DC microgrid for grid connected and islanded operations. IEEE Transactions on Smart Grid, 6(4), 1588-1601.
11. Ding, G., Gao, F., Zhang, S., Loh, P. C., & Blaabjerg, F. (2014). Control of hybrid AC/DC microgrid under islanding operational conditions. Journal of Modern Power Systems and Clean Energy, 2(3), 223-232.
12. Unamuno, E., & Barrena, J. A. (2015). Hybrid ac/dc microgrids—Part I: Review and classification of topologies. Renewable and Sustainable Energy Reviews, 52, 1251-1259.
13. Gao, F., Bozhko, S., Costabeber, A., Patel, C., Wheeler, P., Hill, C. I., & Asher, G. (2016). Comparative stability analysis of droop control approaches in voltage-source-converter-based DC microgrids. IEEE Transactions on Power Electronics, 32(3), 2395-2415.
14. Kotra, S., & Mishra, M. K. (2019). Design and stability analysis of DC microgrid with hybrid energy storage system. IEEE Transactions on Sustainable Energy, 10(3), 1603-1612.

15. Liu, J., Zhang, W., & Rizzoni, G. (2017). Robust stability analysis of DC microgrids with constant power loads. IEEE Transactions on Power Systems, 33(1), 851-860.
16. Tahim, A. P. N., Pagano, D. J., Lenz, E., & Stramosk, V. (2014). Modeling and stability analysis of islanded DC microgrids under droop control. IEEE Transactions on power electronics, 30(8), 4597-4607.
17. Wu, D., Tang, F., Dragicevic, T., Guerrero, J. M., & Vasquez, J. C. (2015). Coordinated control based on bus-signaling and virtual inertia for islanded DC microgrids. IEEE Transactions on Smart Grid, 6(6), 2627-2638.
18. Mohamad, A. M., & Mohamed, Y. A. R. I. (2019). Investigation and assessment of stabilization solutions for DC microgrid with dynamic loads. IEEE Transactions on Smart Grid, 10(5), 5735-5747.
19. Zhang, Z., Yang, X., Zhao, S., Wu, D., Cao, J., Gao, M., ... & Wang, Z. (2022). Large-signal stability analysis of islanded DC microgrids with multiple types of loads. International Journal of Electrical Power & Energy Systems, 143, 108450.
20. Li, Z., & Shahidehpour, M. (2017). Small-signal modeling and stability analysis of hybrid AC/DC microgrids. IEEE Transactions on Smart Grid, 10(2), 2080-2095.
21. Hosseinipour, A., & Hojabri, H. (2020). Small-signal stability analysis and active damping control of DC microgrids integrated with distributed electric springs. IEEE Transactions on Smart Grid, 11(5), 3737-3747.
22. El-Shahat, A., & Sumaiya, S. (2019). DC-microgrid system design, control, and analysis. Electronics, 8(2), 124.
23. Su, M., Liu, Z., Sun, Y., Han, H., & Hou, X. (2016). Stability analysis and stabilization methods of DC microgrid with multiple parallel-connected DC–DC converters loaded by CPLs. IEEE Transactions on Smart Grid, 9(1), 132-142.
24. Guo, L., Zhang, S., Li, X., Li, Y. W., Wang, C., & Feng, Y. (2016). Stability analysis and damping enhancement based on frequency-dependent virtual impedance for DC microgrids. IEEE Journal of emerging and selected topics in power electronics, 5(1), 338-350.
25. Jami, M., Shafiee, Q., & Bevrani, H. (2020). Dynamic improvement of DC microgrids using a dual approach based on virtual inertia. Journal of Modern Power Systems and Clean Energy, 10(3), 667-677.
26. Gui, Y., Han, R., Guerrero, J. M., Vasquez, J. C., Wei, B., & Kim, W. (2021). Large-signal stability improvement of DC-DC converters in DC microgrid. IEEE Transactions on Energy Conversion, 36(3), 2534-2544.
27. Liu, S., Zheng, J., Li, R., Li, X., Fang, W., & Liu, X. (2019, August). Multiple Lyapunov function-based large signal stability analysis of DC microgrid with coordinated control. In 2019 22nd International Conference on Electrical Machines and Systems (ICEMS) (pp. 1-6). IEEE.
28. Mansour, M. Z., Me, S. P., Hadavi, S., Badrzadeh, B., Karimi, A., & Bahrani, B. (2021). Nonlinear transient stability analysis of phased-locked loop-based grid-following voltage-source converters using Lyapunov's direct method. IEEE Journal of emerging and selected topics in Power Electronics, 10(3), 2699-2709.
29. Oshnoei, A., Azzouz, M. A., Awad, A. S., Blaabjerg, F., & Anvari-Moghaddam, A. (2023). Adaptive damping control to enhance small-signal stability of DC microgrids. IEEE Journal of Emerging and Selected Topics in Power Electronics, 11(3), 2963-2978.
30. Wu, H., & Wang, X. (2019). Design-oriented transient stability analysis of PLL-synchronized voltage-source converters. IEEE Transactions on Power Electronics, 35(4), 3573-3589.
31. Simiyu, P., Xin, A., Mouhammed, N., Kunyu, W., & Gurti, J. (2020). Multi-terminal medium voltage DC distribution network large-signal stability analysis. Journal of Electrical Engineering & Technology, 15, 2099-2110.
32. Rachita R. Sarangi,Prakash K. Ray,Asit Mohanty,Shafi Khadem & Sandipan Patra. (2025). Enhancing DC microgrid security: A comprehensive review of protection challenges and solutions. International Journal of Electrical Power and Energy Systems,168,110687-110687.
33. Adly Moustafa & Strunz Kai. (2021). DC microgrid small-signal stability and control: Sufficient stability criterion and stabilizer design. Sustainable Energy, Grids and Networks,(prepublish),100435-.
34. Shashank Shekhar & Aftab Alam. (2024). Adaptive droop control for enhanced stability and robustness in DC microgrids. Computers and Electrical Engineering,120(PA),109649-109649.